Distinguishing attosecond electron–electron scattering and screening in transition metals

Cong Chen[a], Zhensheng Tao[a,1], Adra Carr[a], Piotr Matyba[a,2], Tibor Szilvási[b], Sebastian Emmerich[c], Martin Piecuch[c], Mark Keller[d], Dmitriy Zusin[a], Steffen Eich[c], Markus Rollinger[c], Wenjing You[a], Stefan Mathias[c,3], Uwe Thumm[e], Manos Mavrikakis[b], Martin Aeschlimann[c], Peter M. Oppeneer[f], Henry Kapteyn[a], and Margaret Murnane[a,1]

[a]JILA, Department of Physics, University of Colorado and National Institute of Standards and Technology, Boulder, CO 80309; [b]Department of Chemical and Biological Engineering, University of Wisconsin–Madison, Madison, WI 53706; [c]Research Center OPTIMAS, Department of Physics, University of Kaiserslautern, 67663 Kaiserslautern, Germany; [d]National Institute of Standards and Technology, Boulder, CO 80305; [e]Department of Physics, Kansas State University, Manhattan, KS 66506; and [f]Department of Physics and Astronomy, Uppsala University, 75120 Uppsala, Sweden

Contributed by Margaret Murnane, May 18, 2017 (sent for review April 19, 2017; reviewed by Shaul Mukamel and Xiaoyang Zhu)

Electron–electron interactions are the fastest processes in materials, occurring on femtosecond to attosecond timescales, depending on the electronic band structure of the material and the excitation energy. Such interactions can play a dominant role in light-induced processes such as nano-enhanced plasmonics and catalysis, light harvesting, or phase transitions. However, to date it has not been possible to experimentally distinguish fundamental electron interactions such as scattering and screening. Here, we use sequences of attosecond pulses to directly measure electron–electron interactions in different bands of different materials with both simple and complex Fermi surfaces. By extracting the time delays associated with photoemission we show that the lifetime of photoelectrons from the *d* band of Cu are longer by ∼100 as compared with those from the same band of Ni. We attribute this to the enhanced electron–electron scattering in the unfilled *d* band of Ni. Using theoretical modeling, we can extract the contributions of electron–electron scattering and screening in different bands of different materials with both simple and complex Fermi surfaces. Our results also show that screening influences high-energy photoelectrons (≈20 eV) significantly less than low-energy photoelectrons. As a result, high-energy photoelectrons can serve as a direct probe of spin-dependent electron–electron scattering by neglecting screening. This can then be applied to quantifying the contribution of electron interactions and screening to low-energy excitations near the Fermi level. The information derived here provides valuable and unique information for a host of quantum materials.

attosecond science | high harmonic generation | ARPES | electron–electron interactions

Excited-state electron dynamics in materials play a critical role in light-induced phase transitions in magnetic and charge density wave materials, in superdiffusive spin flow, in catalytic processes, and in many nano-enhanced processes. However, to date exploring such dynamics is challenging both experimentally and theoretically. Using femtosecond lasers in combination with advanced spectroscopies, it is possible to measure the lifetime of excited charges and spins directly in the time domain (1). To date, such studies have been applied to a wide variety of materials, including noble metals and semiconductors (1–4), ferromagnetic metals (5–8), strongly correlated materials (9) and high-T_c superconductors (10, 11). These studies have significantly improved our understanding of the fastest coupled interactions and relaxation mechanisms in matter. However, to date experimental investigations of electron dynamics have been limited to femtosecond timescale processes in materials with low charge densities (9–12) or to Fermi-liquid metals with low excitation energies (<3.0 eV above E_F, where E_F is the Fermi energy) (3–5), due to the visible-to-UV-wavelength photon energies used in these experiments. In this region, two fundamental electron interactions—electron–electron scattering and charge screening due to a rearrangement of adjacent charges—contribute to the signal, making it challenging to independently probe these dynamics. On the theory side, initial studies in the late 1950s were enabled by the seminal Fermi-liquid theory of Landau (13–16). In exciting recent developments using the self-energy formalism of many-body theory and the random phase approximation, calculations of electron–electron interaction in materials—that include the material band structure—have now become possible (17–22). Thus, experimental approaches that can distinguish between different electron–electron interactions, particular with band specificity, are very important and timely.

High harmonic generation (HHG) provides attosecond pulses and pulse trains that are perfectly synchronized to the driving laser and that are ideal for probing the fastest coupled charge and spin dynamics in atoms, molecules, and materials (23–33). To date, two approaches have been used to probe attosecond electron dynamics in matter through photoemission, taking advantage of laser-assisted photoemission sidebands (24, 25). For atoms, because the energy separation between different states is large, attosecond streaking using isolated attosecond pulses (with an energy resolution of several electronvolts) has been applied very successfully (26, 27). The same approach has also been used to measure the transit time for a photoelectron to be emitted

Significance

Electron–electron interactions are among the fastest processes in materials that determine their fascinating properties, occurring on attosecond timescales on up (1 as = 10^{-18} s). The recent development of attosecond angle-resolved photoemission spectroscopy (atto-ARPES) using high harmonic generation has opened up the possibility of probing electron–electron interactions in real time. In this paper, we distinguish electron–electron screening and charge scattering in the time domain in individual energy bands within a solid. These results open up new possibilities for probing fundamental electron–electron interactions in a host of materials including magnetic, superconducting, and advanced quantum materials.

Author contributions: H.K. and M. Murnane designed research; C.C., Z.T., A.C., P.M., T.S., S. Emmerich, M.P., M.K., D.Z., S. Eich, M.R., W.Y., S.M., U.T., M. Mavrikakis, M.A., P.M.O., H.K., and M. Murnane performed research; C.C. and Z.T. analyzed data; C.C., Z.T., P.M.O., H.K., and M. Murnane wrote the paper; T.S. conducted the band structure calculation under the supervision of M. Mavrikakis; M.K. performed the sample growth; and U.T. and M. Mavrikakis wrote the theory portion of the manuscript.

Reviewers: S.M., University of California, Irvine; and X.Z., Columbia University.

The authors declare no conflict of interest.

Freely available online through the PNAS open access option.

[1]To whom correspondence may be addressed. Email: Zhensheng.Tao@colorado.edu or Margaret.Murnane@colorado.edu.

[2]Present address: Department of Physics, Umeå University, SE-901 87 Umea, Sweden.

[3]Present address: Physikalisches Institut, Georg-August-Universität Göttingen, 37077 Goettingen, Germany.

This article contains supporting information online at www.pnas.org/lookup/suppl/doi:10.1073/pnas.1706466114/-/DCSupplemental.

from the surface of a material. The RABBITT method (28–30) (reconstruction of attosecond beating by interference of two-photon transitions) has also been very successfully applied to atomic and material samples, where quantum interferences between neighboring two-photon transition pathways can modulate these sidebands as a function of the relative time delay between the HHG pump and IR probe pulses: Any time delay in photoemission from different initial or final states will lead to a phase delay in the interferograms (28, 31).

Very recently, by combining attosecond HHG pulse trains with time- and angle-resolved photoemission (ARPES), we demonstrated the ability to resolve attosecond electron dynamics in different individual final states in materials, with ≈20-as time resolution. We used attosecond-ARPES to measure a photoelectron lifetime of ∼210 as, which was measured for a final state that coincides with an unoccupied excited state in the band structure of Ni (32, 33). We also showed that the photoelectron lifetime sensitively depends on the band dispersion of the material (i.e., the photoelectron emission angle). That work demonstrated that atto-ARPES can probe intrinsic properties of materials. A great advantage of atto-ARPES is that it achieves good energy resolution (<0.3 eV), to enable band-selectivity as well as angle-resolved studies, combined with the ability to change the HHG polarization, which are all critical for harnessing photoemission selection rules. This makes it possible, in principle, to selectively capture electron dynamics in different initial or final bands in many materials, because the typical separation between neighboring valence bands is <1eV.

Here, we use sequences of attosecond pulses coupled with time-, energy-, polarization-, and angle-resolved photoelectron spectroscopy (atto-ARPES) to distinguish electron–electron interactions for electrons excited from different initial bands during the photoemission process. The high photoelectron energies ($E - E_F$ >20 eV), combined with attosecond time resolution, allows us to independently measure electron–electron scattering in metals with simple and complex Fermi surfaces, without the influence of screening. To achieve this, we extract the time delays associated with photoemission from individual valence bands in Ni(111) and Cu(111). We find that the lifetime of photoelectrons from a *d* band of Cu is longer by ∼100 as compared with the lifetime of those from the same band of Ni. We attribute this difference to the fact that the *d* band in Ni is not fully occupied, resulting in enhanced electron–electron scattering and hence a shorter photoelectron lifetime (Fig. 1*A*). Then, using a spin-dependent scattering model to compare electron–electron interactions in Cu and Ni, we show that the photoexcited electron lifetime in Ni involves enhanced electron–electron scattering throughout the energy range from 0.5 eV to 40 eV. Moreover, because screening influences high-energy photoelectrons (≈20 eV) significantly less than low-energy photoelectrons (20, 22), they can serve as a direct probe of spin-dependent electron–electron scattering. The resulting Coulomb interaction information we extract is applicable across a broad energy range—from the Fermi energy on up—and can separate and quantify the contribution of screening to low-energy excitations, where both screening and scattering contribute to the signal. Our atto-ARPES approach

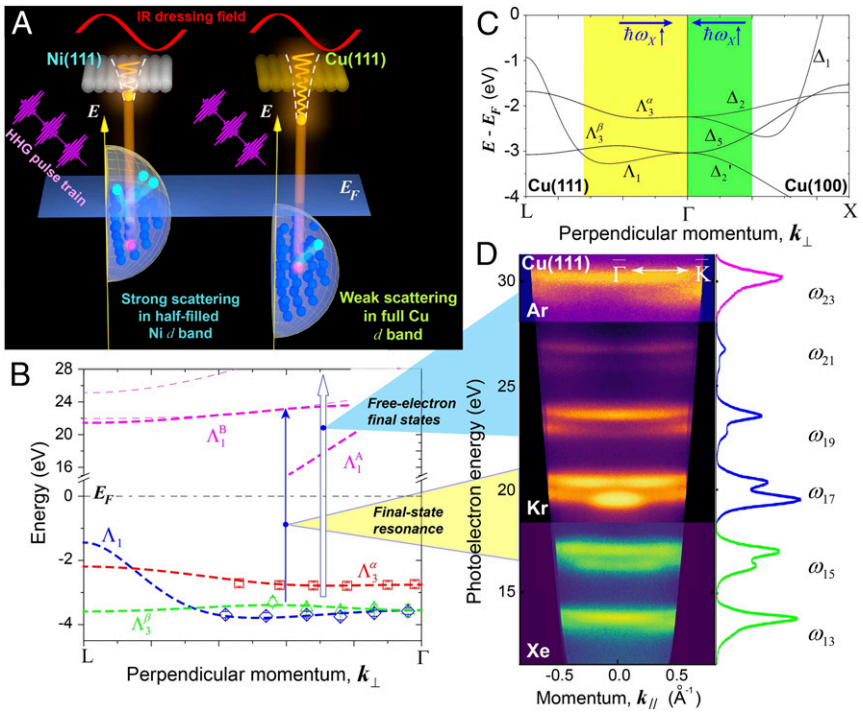

Fig. 1. Influence of the material band structure on attosecond electron dynamics. (*A*) Illustration of the photoemission process from Cu(111) and Ni(111) surfaces. Using HHG pulse trains, photoelectrons are excited either from a Cu(111) or Ni(111) surface. Due to the different band structure in these two materials, photoelectrons from Ni(111) experience more electron–electron scattering, which reduces the lifetime of photoelectrons by 100 as compared with Cu(111) as they escape from the material surface. The enhanced scattering also reduces the inelastic mean free path. (*B*) Band structure of Cu(111) along the Γ–L direction from DFT calculation (dashed lines), compared with experimental results of band mapping [open symbols; see *S3. Static HHG Photoelectron Spectra Analysis of Cu(111)*]. The interband transition $\Lambda_3^\beta \rightarrow \Lambda_1^B$ is highlighted by the blue arrow, which corresponds to the spectral enhancement of the photoelectron spectrum at harmonic orders ω_{15} and ω_{17} as shown in *D*. (*C*) Band structure of Cu along the Γ–L direction for Cu(111), and Γ–X for Cu(100), showing the evolution of the Λ bands to Δ bands across the Γ point. Due to the photoemission selection rules (34), transitions from Δ_2 bands are forbidden in the normal emission geometry from Cu(100). The colored areas indicate the perpendicular momentum regions measured in our experiments. Blue arrows indicate the direction in which the HHG photon energy ($\hbar\omega_X$) increases. (*D*) Static ARPES spectra excited by an s-polarized HHG field, generated using different noble gases (Xe, Kr, and Ar). Photoemission from two initial bands (Λ_3^α and Λ_3^β) can be clearly distinguished.

thus makes it possible to independently distinguish the fastest electron–electron scattering and screening dynamics in metals on attosecond time scales, providing valuable information for a host of magnetic materials.

Experiment

The concept behind our study is shown in Fig. 1*A*. Most of the output of a near-IR femtosecond laser is used to generate high harmonics in various noble gases (Xe, Kr, and Ar), which are then focused onto single crystal Cu(111) and Ni(111) surfaces. In the spectral domain, these harmonics span ∼15–45 eV (corresponding to 11ω–27ω), each with a linewidth of ∼0.3 eV, and separated by $2\omega_L \approx 3.2$ eV, where ω_L is the frequency of the driving IR laser. The residual phase-locked laser field is used to simultaneously irradiate the material together with a high harmonic field, which induces sidebands of the photoelectron peaks corresponding to the absorption or emission of an IR laser photon. The photoelectron spectrum is then collected using a hemispherical photoelectron analyzer (Specs Phoibos 100). Note that it has already been shown that RABBITT and attosecond-streaking yield the same temporal information about the photoemission process (31), whereas ARPES adds significant advantages of band specificity (33). Moreover, by simultaneously measuring two photoelectron wavepackets from different initial states excited by the same harmonic orders we can eliminate the influence of the HHG phase (28).

The band structure of Cu(111) is plotted in Fig. 1*B*. Similar to Ni(111) (33), there are three valence bands along the Γ–L direction of Cu(111): the Λ_3^α band with a binding energy of ∼2.8 eV, Λ_3^β with ∼3.5 eV, and Λ_1 with ∼3.8 eV. By using an s-polarized HHG field we can exclusively excite photoelectrons from the Λ_3^α and Λ_3^β bands (34, 35). The band-mapping results are also plotted in Fig. 1*B*, which shows a strong dispersion of the photoemission peaks as a function of photon energy, indicating that photoemission from bulk states contributes to the signal [*S3. Static HHG Photoelectron Spectra Analysis of Cu(111)*]. In our experiments, photoemission from the Cu(100) surface is also measured, which corresponds to a band structure along Γ–X direction (Fig. 1*C*). As shown in Fig. 1*D*, photoemission dipole transitions couple different initial and final states (bands) of Cu(111) that can be selected using different harmonic orders and polarizations, by harnessing photoemission selection rules (34, 35). To distinguish the influence of wavefunction localization (excited bulk states vs. free-electron final states) as well as the influence of the fundamental electron interactions on the photoelectron lifetimes, we first identify where the final-state resonances occur in Cu(111). The spectral intensity of Λ_3^β band photoelectrons excited by the s-polarized HHG field is plotted in Fig. 2*A*. A strong enhancement of the spectral intensity peaked at the resonant photon energy of ∼26 eV can be observed, which can be attributed to the interband transition from the Λ_3^β initial band to the excited Λ_1^B final band (Fig. 1*B*). The Lorentzian linewidth is $\gamma_{\text{spec}} = 2.13 \pm 0.65$ eV (Fig. 2*A*), which is consistent with the linewidth recently obtained using high-resolution photoemission at a synchrotron radiation source (36). The predicted final-state lifetime is therefore given by $\tau_{\text{spec}} = \hbar/\gamma_{\text{spec}} = 309 \pm 94$ as.

The photoemission time delay $\tau_{PE}(\Lambda_3^\beta) - \tau_{PE}(\Lambda_3^\alpha)$ at the Γ point can be extracted from the RABBITT interferogram (Fig. 2*D*) and is summarized in Fig. 2*B*. The quantum paths involved in RABBITT interference are illustrated in Fig. 2*C*. These interferograms (Fig. 2*D*) were obtained by integrating the photoelectron spectra over ±2.5° around the Γ point (normal-emission direction). Comparing Fig. 2 *A* and *B*, we find that $\tau_{PE}(\Lambda_3^\beta) - \tau_{PE}(\Lambda_3^\alpha)$ at the Γ point reaches its maximum value $\tau_{\text{chron}} = 291 \pm 48$ as at the resonant photon energy for the interband transition $\Lambda_3^\beta \rightarrow \Lambda_1^B$(Fig. 1*B*), which is in good agreement with $\tau_{\text{spec}} \approx 309 \pm 94$ as. This agreement indicates that the lifetime of photoelectrons emitted from the initial Λ_3^α band $[\tau_{PE}(\Lambda_3^\alpha)]$ is short at the Γ point. Considering the fact that the spectral intensity of Λ_3^α is a smooth function of photon energy (*Supporting Information*, Fig. S4), it allows us to directly assign the measured time delay to the lifetime of photoelectrons from the Λ_3^β band. Compared with Ni(111) (33), the resonant linewidth from the initial Λ_3^β band in Cu is narrower, which is consistent with the longer lifetime measured in the time domain (291 ± 48 as for Cu vs. 212 ± 30 as for Ni).

For photoemission through free-electron final states (away from any final-state resonances, >25 eV in Fig. 3*A*), we find that the photoelectron lifetime from the Λ_3^β band of Cu(111) is ∼100 as in the normal-emission geometry. Moreover, this lifetime is a smooth function of the final-state energy (Fig. 3*A*). The associated time delay can be clearly seen in the experimentally measured interferograms of Cu(111) as an obvious phase shift in the oscillations of the RABBITT quantum interferences (Fig. 3*B*), which interestingly is absent in Ni(111) for free-electron final states (33). We note that we can exclude the possibility that the finite photoelectron lifetime in this energy range in Cu(111) is caused by another final-state resonance because we did not observe any photoelectron yield enhancement in this energy range (Fig. 2*A*), and because it exhibits little momentum (angle) dispersion—unlike the lifetime on resonance (Fig. 3*C*). To further reinforce this conclusion, we also measured the photoemission time delay between the Δ_5 and Δ_1 bands along the Γ–X direction for Cu(100) as the two Λ_3 bands cross the Γ point of the Brillouin zone (BZ) [Fig. 1*C*; see *S2. Static ARPES Spectra of Cu(111) and Cu(001)* for more details]. As shown in Fig. 2*B*, a similar lifetime difference between Δ_5 and Δ_1 band photoelectrons was observed on the Cu(100) surface when there is no spectral resonance. Excluding final-state effects, the ∼100 as lifetime difference of photoelectrons from the Λ_3^β band for Cu(111) and Ni(111) must be attributed to differences in the fundamental electron–electron interactions experienced by the high-energy photoexcited electrons during photoemission from these two materials.

Discussion

The photoexcited electron lifetime for free-electron final states is mainly determined by the competition between dynamic screening and inelastic electron–electron scattering during the photoemission process (18). This is because for highly excited electronic states (>20 eV) other decay channels, including scattering with photoholes, phonons, and impurities, are expected to have negligible contributions. In Fig. 3*A* we compare our measured photoelectron lifetime from the Λ_3^β band of Cu to two empirical models [Goldmann et al. (37) and Eberhardt and coworkers (36)] that are based on bulk excited-state linewidths, as well as a free-electron gas (FEG) model with $r_s = 2.67$ for Cu (18), where r_s is the electron-density parameter defined for an electron density n by $n = 3/(4\pi r_s^3)$. As shown in Fig. 3*A*, both empirical models agree well with the photoelectron lifetime on resonance (SB16) as expected; however, they overestimate the photoelectron lifetime off-resonance. This is not surprising—the Goldmann and Eberhardt models are derived from a linewidth analysis of photoemission and inverse photoemission experiments (36, 37) that are mainly based on contributions from resonant (bulk final state) excitations. Compared with steady-state photoemission and inverse photoemission studies, our time-domain approach has unique advantages that allow us to measure the intrinsic high-energy photoelectron lifetime at arbitrary energies (including transitions both on and off final-state resonance). Note that the FEG model cannot reproduce the photoelectron lifetime on resonance, which is also not surprising because it does not account for the real band structure of the material. Most interestingly, the FEG model matches the off-resonance (i.e., free-electron final-state) lifetime measured on Cu(111) very well, but not for Ni(111), which is ∼100 as shorter. Note that this trend is very different from the hot-electron lifetimes measured at low energy (<3 eV above E_F), which exhibit a strong

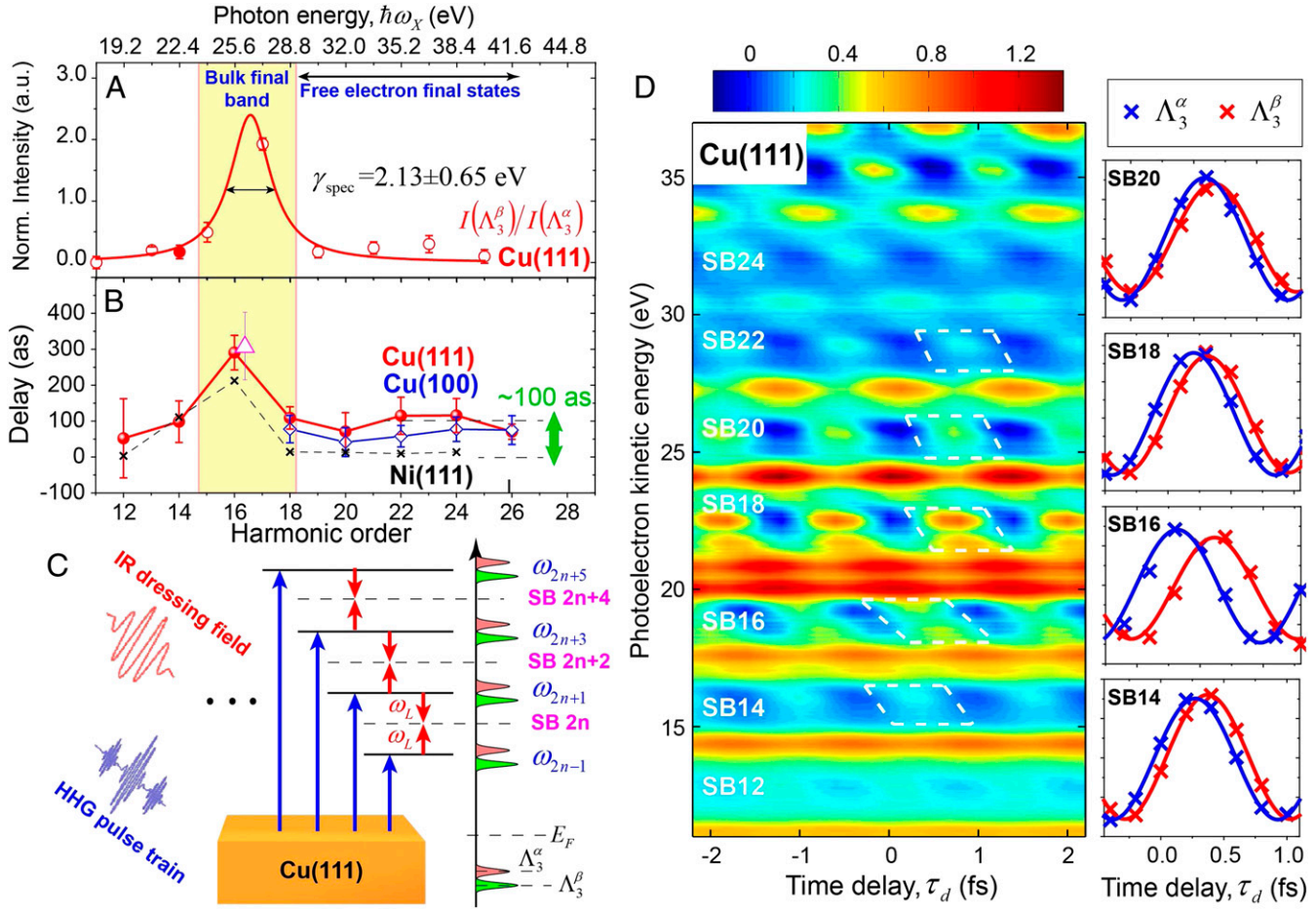

Fig. 2. Comparison of photoelectron lifetimes in Cu(111) and Ni(111) for photoemission either into excited states (on resonance, ≈25 eV) or into free-electron states (off resonance). (*A*) Normalized spectral intensity of the Cu(111) Λ_3^β band as a function of photon energy. The filled symbol (14th order) is obtained from HHG driven by 390-nm laser field. The red solid line represents the Lorentzian fitting to the spectral intensity, which yields a linewidth of 2.13 ± 0.65 eV. The center of Lorentzian fitting is given by the final-band energy obtained from DFT calculation (Fig. 1*B*). (*B*) Photoemission time delay $\tau_{PE}(\Lambda_3^\beta) - \tau_{PE}(\Lambda_3^\alpha)$ as a function of photon energy for both Cu(111) and Ni(111) surfaces. The time delay $\tau_{PE}(\Delta_5) - \tau_{PE}(\Delta_1)$ measured for a Cu(100) surface is also plotted for comparison. The open triangle represents the lifetime derived from the linewidth in *A*. (*C*) Illustration of the quantum-path interference in RABBITT measurements. Electrons from two initial states (Λ_3^α and Λ_3^β) are excited by multiple harmonic orders into different final states. By absorbing and emitting one additional IR photon (ω_L), quantum-path interference causes spectral modulation at the sidebands (SB) in between neighboring harmonic orders. (*D*) Two-dimensional map of photoelectron spectral intensity as a function of photoelectron energy and HHG-laser field time delay τ_d. The relative time delay between photoelectrons from Λ_3^β and Λ_3^α initial bands are highlighted as large offsets in oscillations in the sideband region by white dashed boxes. (*Right*) One-dimensional lineouts for the spectral modulations with angular integration of ±2.5° around the Γ point of photoelectrons from Λ_3^β and Λ_3^α initial bands in the selected sideband regions.

deviation from the FEG model due to the added presence of screening of *d*-band electrons (17, 19).

The absence of electron screening effects in high-energy photoemission can be understood by considering two different aspects. First, screening of *d* band electrons can be estimated by considering an effective dielectric constant $\varepsilon_d = 1 + \delta\varepsilon_d$, which is induced by the polarizable background of *d* electrons. At low energies, the corrected lifetime is larger than the value predicted by the FEG model by $\sqrt{\varepsilon_d}$ (38–40). As pointed out by Quinn (41, 42), $\delta\varepsilon_d$ reduces as a function of excitation photon energy. As a result, the variation of the photoelectron lifetime due to *d*-electron screening is estimated to be only a few percent of the FEG lifetime at energies >20 eV (*S8. Approximate Estimate of d-Electron Screening*). Second, on ∼100-as time scales, we also need to consider the dynamics of electron screening in metals. As shown in previous theoretical studies, the buildup of charge screening in metals is not instantaneous but takes approximately half of a plasma period to fully develop (43), which corresponds to ∼200 as in both Cu and Ni. Because the off-resonance photoelectron lifetimes are much less than this, it seems that photoelectrons from Cu (and Ni) escape before dynamic screening can influence the photoelectron lifetime in this energy range. As a result, dynamic electron screening has negligible influence on the photoelectron lifetimes at energies >20 eV.

However, the ∼100-as lifetime difference between photoelectrons from the *d* bands of Cu and Ni can be attributed to the differences in the band structure of these materials, which results in different electron–electron scattering rates between photoelectrons and other electrons in the conduction bands during photoemission. Here, we consider a high-energy photoexcited electron with energy E above E_F. This electron decays into a lower energy state E' by exciting one of the other electrons in the band (a scattering partner) from its original state ε into an unoccupied state above E_F, $\varepsilon + \Delta$, where $\Delta = E - E'$ is the energy transfer (Fig. 4*A*). We note that the scattering process illustrated in Fig. 4*A* is responsible for removing photoelectron signal from our measurement. Thus, the experimentally measured photoelectrons are those that escape without scattering; nevertheless,

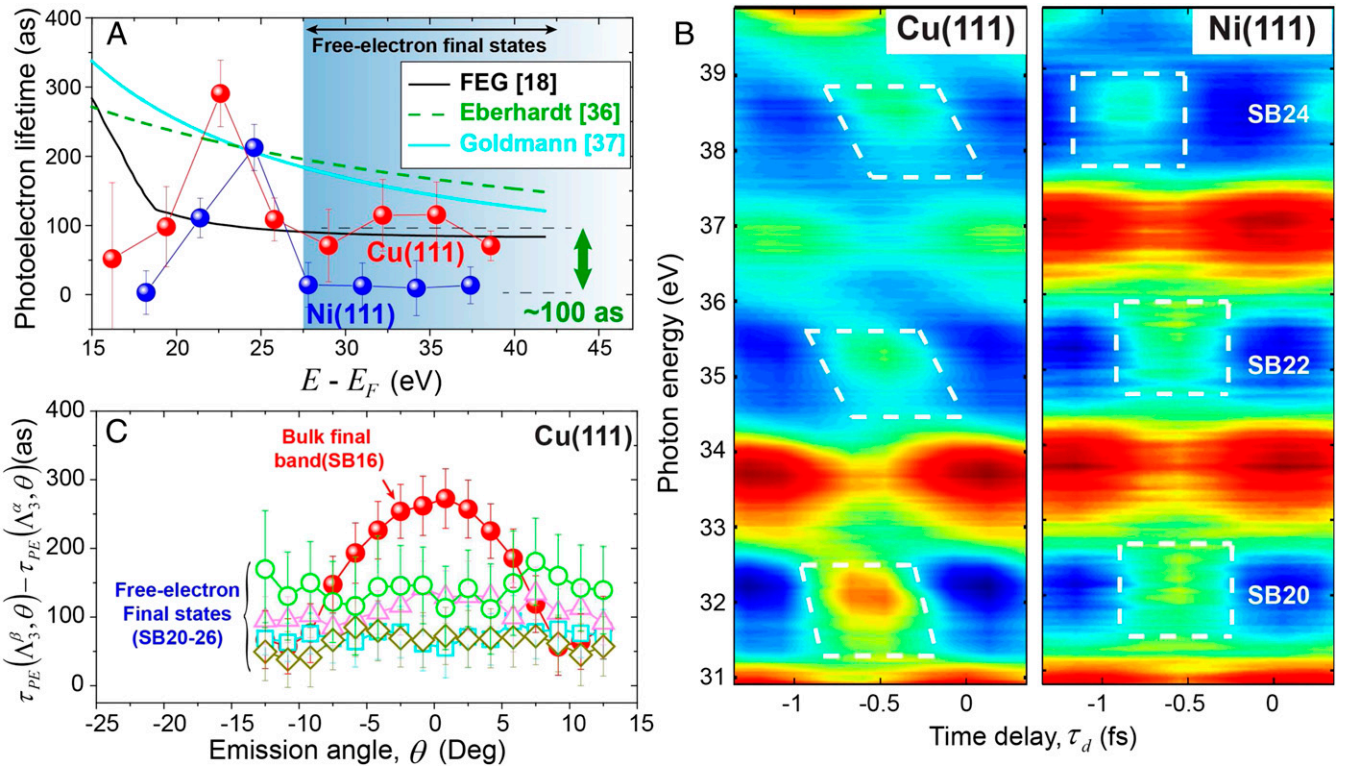

Fig. 3. Origin of different photoelectron lifetimes for photoemission into free-electron final states for Cu and Ni. (*A*) Photoelectron lifetime emitted from Λ_3^β band measured using atto-ARPES as a function of the final-state energy ($E - E_F$) for both Cu(111) and Ni(111), in comparison with the FEG model (black) (18), Goldmann et al. (cyan) (37) and Eberhardt and coworkers (green dashed) (36) models. The lifetime corresponding to free-electron final states are highlighted in the colored region. (*B*) Interferograms for sidebands 20–24 (off-resonance, away from final-band resonance) measured from Cu(111) and Ni(111) (33) surfaces. Large offsets in the sideband regions can be observed in the Cu(111) data, as highlighted by the white dashed boxes. Such offsets are absent for Ni(111). (*C*) Angle-dependent photoemission time delay of $\tau_{PE}(\Lambda_3^\beta,\theta) - \tau_{PE}(\Lambda_3^\alpha,\theta)$ measured on Cu(111), which clearly shows the difference between a resonant transition to a bulk final band (sideband 16) and those to free-electron final states (sideband 20, square; sideband 22, triangle; sideband 24, circle; and sideband 26, diamond).

the lifetimes of these electrons are influenced by scattering within the occupied bands and experience different phase shifts in our RABBITT measurement. The scattering rate (which will correspond to the inverse of the lifetime τ_σ) can be calculated using Fermi's golden rule in the random-$\boldsymbol{k}$ approximation (6, 44–46) (*S7. Spin-Dependent Scattering Model*),

$$\frac{1}{\tau_\sigma(E)} = \frac{\pi}{\hbar}\int_{E_F}^{E} dE' \Bigg\{ \sum_{\beta=s,p,d} \rho_\sigma^{\beta,>}(E') \sum_{\alpha=s,p,d} \int_{E_F-\Delta}^{E_F} d\varepsilon \times \left[\rho_\sigma^{\alpha,<}(\varepsilon)\rho_\sigma^{\alpha,>}(\varepsilon+\Delta) 2|M^{\sigma\sigma}|^2 + \rho_{\bar\sigma}^{\alpha,<}(\varepsilon)\rho_{\bar\sigma}^{\alpha,>}(\varepsilon+\Delta)|M^{\sigma\bar\sigma}|^2 \right] + \sum_{\beta=s,p,d} \rho_{\bar\sigma}^{\beta,>}(E') \sum_{\alpha=s,p,d} \int_{E_F-\Delta}^{E_F} d\varepsilon\, \rho_{\bar\sigma}^{\alpha,<}(\varepsilon)\rho_\sigma^{\alpha,>}(\varepsilon+\Delta)|M^{\sigma\bar\sigma}|^2 \Bigg\}, \quad [1]$$

where $\sigma = \uparrow,\ \downarrow$ is the electron spin ($\bar\sigma$ is the opposite spin to σ), α and β designate the *s*-, *p*-, or *d*-like wavefunction of the scattering partners and the photoexcited electrons, respectively, and

$$\rho_\sigma^{\alpha,>}(E) = [1 - f(E)]\rho_\sigma^\alpha(E)$$

$$\rho_\sigma^{\alpha,<}(E) = f(E)\rho_\sigma^\alpha(E), \quad [2]$$

where $f(E)$ is the Fermi–Dirac distribution function and $\rho_\sigma^\alpha(E)$ is the spin-dependent density of states (DOS) of the α orbital that is obtained from a density-functional theory (DFT) calculation (Fig. 4*C*, *Inset*). We note that because the unoccupied states above the Fermi energy in Ni are dominated by electronic states with minority-spin polarization (↓), spin-dependent scattering needs to be taken into account, which results in spin-dependent excited-electron lifetime in the ferromagnetic materials such as Ni (5, 6, 46). Here $M^{\sigma\sigma}$ is the spin-dependent, crystal momentum- and orbital-averaged Coulomb matrix element, assuming $M^{\uparrow\uparrow} = M^{\downarrow\downarrow}$ and $M^{\uparrow\downarrow} = M^{\downarrow\uparrow}$ (see *S7. Spin-Dependent Scattering Model* for more details). Indeed, as shown in Fig. 3*C*, we verified experimentally that the assumption of a momentum-averaged Coulomb matrix element M is valid, as originally suggested by Berglund and Spicer (44). Similar models have also been successfully used to explain the hot-electron lifetimes of intermediate states measured using time-resolved two-photon photoemission (Tr-2PPE) (6, 46). Assuming $\rho_\uparrow = \rho_\downarrow = \rho$ and $M^{\uparrow\uparrow} = M^{\uparrow\downarrow} = M$, Eq. **1** is simply reduced to $\frac{1}{\tau(E)} = \frac{2\pi}{\hbar}\rho^3|M|^2(E - E_F)^2$, which is the well-known $(E - E_F)^{-2}$ scaling of hot-electron lifetimes excited close to the E_F (44).

We first evaluate the influence of the DOS on the available phase space for scattering by assuming $M^{\uparrow\uparrow} = M^{\uparrow\downarrow} = 1.0$ in Eq. **1**. As shown in Fig. 4*B*, *Inset*, the phase space increases monotonically as a function of the photoexcited electron energy above E_F for both Ni and Cu, and indeed the phase space of Ni is larger than that of Cu in the energy range of our experiments, indicating that a higher scattering rate and a shorter photoelectron lifetime would indeed be expected. The additional phase space of Ni is dominated by the unoccupied DOS above E_F, as evidenced by the fact that the available phase space of Ni moves closer to Cu as its DOS is down-shifted by 1.8 eV to artificially remove the peaked unoccupied DOS (dashed line in Fig. 4*B*,

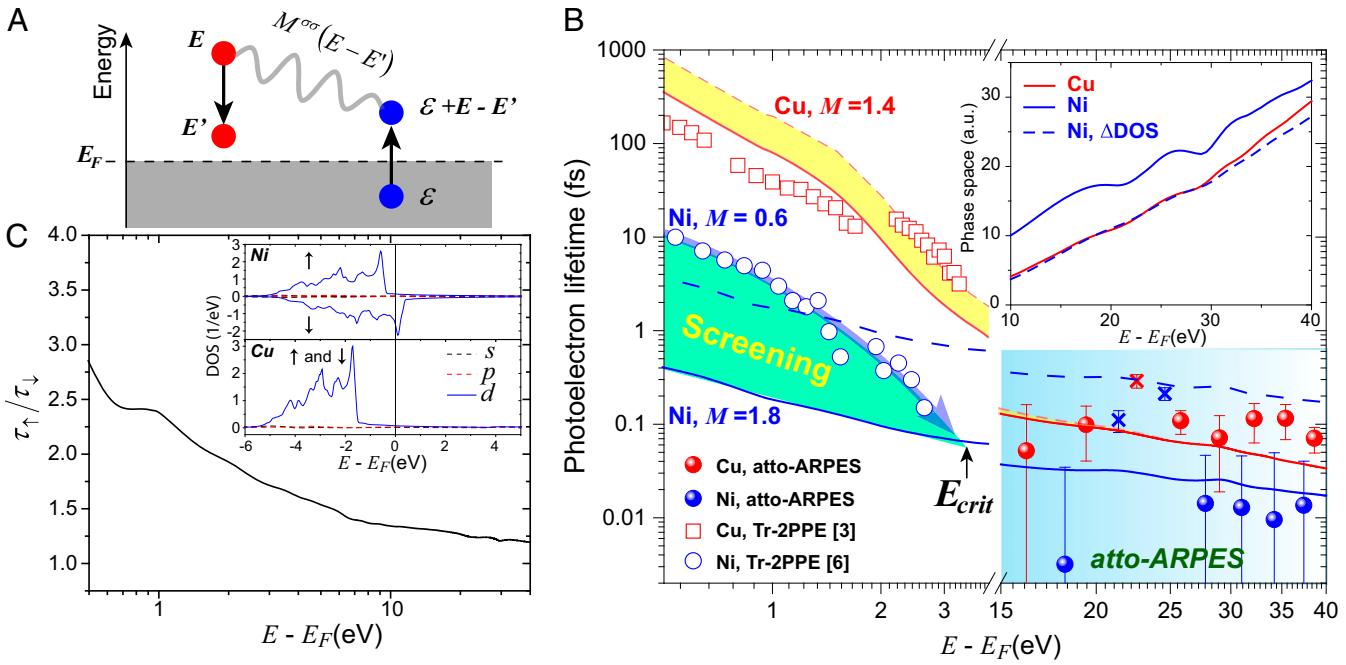

Fig. 4. Spin-dependent model of electron–electron scattering. (*A*) Illustration of the electron–electron scattering process described by Eq. **1**. The photoexcited electron (red circle) can decay by exciting another unexcited electron (blue circle) to a state above E_F. $M^{\sigma\sigma}(E-E')$ is the Coulomb matrix element, which we find is mostly constant for Cu (at 1.4) across a broad energy range but varies for Ni due to stronger screening at low energies. (*B*) Comparison between the spin-dependent scattering model [red (Cu) and blue (Ni)] and the experimentally measured lifetime of photoexcited electrons in Cu and Ni. The low-energy data (0.5–3 eV) are measured using Tr-2PPE method, extracted from ref. 3 for Cu and from ref. 6 for Ni. The high-energy data (15–40 eV) are directly measured in our experiment using atto-ARPES. The data that overlap final-state resonances in both materials are represented by crosses to distinguish them from the off-resonant results of interest here. The yellow area estimates *d*-electron screening effects by considering the optical constants of Cu (47). The experimentally measured low-energy electron lifetime approaches the bare electron–electron scattering limit (solid blue line, $M = 1.8$ for Ni) at an energy $E_{crit} \sim 3$ eV. (*Inset*) The phase space of the two materials calculated from Eq. **1**, assuming $M^{\uparrow\uparrow} = M^{\uparrow\downarrow} = 1.0$. The blue dashed line (Ni, ΔDOS) is the results with the DOS of Ni downshifted by 1.8 eV. (*C*) Lifetime ratio $\tau_\uparrow/\tau_\downarrow$ as a function of excited electron energy ($E - E_F$) for Ni obtained using Eq. **1**. (*Inset*) Spin and orbital-dependent DOS of Ni and Cu obtained from DFT calculations.

Inset). Fig. 4*B* plots the experimentally measured and theoretically calculated lifetimes of photoexcited electrons from 0.5 to 40 eV. Although the focus of this work is on photoelectron lifetimes in the high-energy >20-eV region, a comparison with Tr-2PPE data allows us to gain valuable physical insights. In general, electron–electron Coulomb interactions are energy-dependent due to different screening properties at different energies in a material (44). Here, for convenience, we assume the Coulomb matrix element M is a constant and select values by fitting to the experimental data. To further determine the Coulomb matrix element, we compare the photoexcited electron lifetimes measured using spin-integrated Tr-2PPE on Cu (3) and Ni (6) with our atto-ARPES results and models. For Cu, we have $M^{\uparrow\uparrow} = M^{\uparrow\downarrow} = M$, because the DOS for electrons with majority (↑) and minority (↓) spins are the same. For Ni, as shown in Fig. 4*C*, *Inset*, there are spin-dependent DOS differences, so we assume $|M^{\uparrow\uparrow}/M^{\uparrow\downarrow}| = 0.5$ and $M = \sqrt{\frac{|M^{\uparrow\uparrow}|^2 + |M^{\uparrow\downarrow}|^2}{2}}$ to get agreement with the spin-dependent electron lifetime measured at low energies (6). The spin-averaged excited electron lifetime $\tau = \frac{2\tau_\uparrow\tau_\downarrow}{\tau_\uparrow + \tau_\downarrow}$ is plotted in Fig. 4*B* as solid lines for Cu and Ni, and Fig. 4*C* plots the ratio between spin-up and spin-down electron lifetimes ($\tau_\uparrow/\tau_\downarrow$). Most interestingly, we find that the photoexcited-electron lifetime in Cu can be explained by a mostly energy-independent Coulomb matrix element ($M = 1.4$) throughout the entire energy range from 0.5 to 40 eV. The presence of the *d*-band screening in the low energy range (<3 eV) is well known for Cu, which increases the lifetime by approximately a factor of 2.5 (17, 47). In stark contrast, our atto-ARPES measurements suggest a stronger energy dependence of the Coulomb matrix element in Ni: $M = 1.8$ is best for high-energy photoelectrons and is close to that observed in Cu, whereas $M = 0.6$ is best for low-energy photoelectrons, which are influenced by both screening and scattering.

Considering that electron screening does not have a strong influence on the photoelectron lifetime in the high energy range (20, 22), we can extract the influence of the bare electron–electron Coulomb interactions (no screening) at high energies and extend the corresponding matrix element to the low energy range (the solid blue line in Fig. 4*B*). The measured lifetime at low energy in Ni is more than one order of magnitude longer than the bare electron–electron scattering limit, as shown in Fig. 4*B*. Most interestingly, we find that the experimentally measured low-energy excited electron lifetime in Ni gradually approaches the bare electron–electron scattering limit (solid blue line in Fig. 4*B*) defined by our atto-ARPES measurement at an energy $E_{crit} \sim 3$ eV above E_F. This further corroborates our findings, because screening is expected to diminish at these higher energies (22). Comparing Cu and Ni, our results strongly suggest the presence of enhanced electron screening in Ni at low energies, which can be attributed to the high DOS at the Fermi energy based on our DFT calculations (Fig. 4*C*, *Inset*) (6). From the above, we conclude that atto-ARPES can extend measurements of photoexcited-electron lifetimes to higher energies (>20 eV) to distinguish and quantify fundamental electron interactions such as electron scattering and screening, as well as the influence of resonant interband transitions. Compared with other approaches, atto-ARPES also has the unique ability to distinguish band-specific electron–electron scattering for direct comparison with theory and can exclude other contributions such as hot electrons and intermediate-state refilling (6, 8, 48).

Finally, we note that spin-dependent electron–electron scattering in ferromagnetic materials is responsible for many interesting

phenomena, including laser-induced demagnetization (8), superdiffusive spin transport, and giant magnetoresistance (49). Low-energy spin-dependent electron lifetimes have been studied, providing much valuable information (5, 6). However, to date it has not been possible to experimentally isolate electron–electron scattering, due to strong contributions to the measured lifetimes from electron screening from localized *d*- and *f*-band electrons, as well as contributions from other interactions (e.g., phonons and impurities). By probing high-energy photoelectron lifetimes, where electron screening becomes negligible, spin-resolved atto-ARPES could probe spin-dependent electron–electron scattering, which could help uncover fundamental magnetic properties.

Conclusion

In conclusion, we show that attosecond electron interactions in metals can be studied using energy-, polarization-, and angle-resolved atto-ARPES, allowing us to distinguish the contributions of occupied and unoccupied bands to the photoelectron lifetimes. Strong electron–electron scattering in the unfilled *d* band of Ni decreases the lifetime of photoelectrons by ∼100 as relative to the photoelectrons emitted from the same band of Cu. Most interestingly, we find that dynamical screening influences high-energy photoelectrons much less than low-energy photoelectrons and is different for Cu and Ni due to the difference in material band structure. As a result, spin-dependent atto-ARPES with high-energy excitation is a unique tool to exclusively study the fundamental processes of spin-dependent electron–electron scattering in magnetic materials and also to quantify the contributions of scattering and screening for low-energy excitations. In the future, atto-ARPES can also be used to extract valuable information about fundamental electron–electron interactions in a host of materials including strongly correlated materials and modern quantum materials.

Methods

We use laser-assisted photoemission and RABBITT to measure the photoelectron lifetimes for different initial and final states. Photoemission from the solid surface is induced by attosecond pulse trains from HHG. The HHG pulse trains are generated in a 150-μm-diameter, 1-cm-long, gas-filled capillary waveguide, driven by ∼2 mJ, 26-fs laser pulses at 780 nm wavelength from a Ti:sapphire amplifier system. We use different noble gases (Xe, Kr, and Ar) to cover a broad extreme ultraviolet (EUV) photon energy range from 16 to 42 eV (corresponding to HHG orders 11–27). A phase-locked linearly polarized IR probe is recombined collinearly with the HHG pulse trains and focused onto the surface with a FWHM spot size of 250 μm and peak intensity of 2.8×10^{11}W/cm^2. The polarization of the IR probe is p-polarized for all our measurements. In the presence of both the attosecond pulse trains and the IR probing field, the angle-resolved photoelectron spectra are modulated as a function of the pump-probe time delays due to quantum-path interference (RABBITT, see Fig. 2*C*), which is recorded by a hemispherical photoelectron analyzer.

ACKNOWLEDGMENTS. We thank J. Rusz, A. Becker, C. Smallwood, G. Mancini, and C. Powell for helpful discussions. This work was done at JILA. This work was supported by the NSF through JILA Physics Frontiers Center Grant PHY-1125844 and Gordon and Betty Moore Foundation EPiQS Award GBMF4538 and Department of Energy (DOE) Office of Basic Energy Sciences X-Ray Scattering Program Award DE-SC0002002 for the spin-dependent scattering aspect of this work (all to M. Murnane and H.K.). Work at University of Wisconsin–Madison was supported by the Air Force Office of Scientific Research Grant FA9550-16-1-0141 (to T.S. and M. Mavrikakis). This work was also supported by the Swedish Research Council and Wallenberg Foundation Grant 2015.0060 (to P.M.O.); NSF Grant PHY 1464417, the DOE Chemical, Geosciences, and Biosciences Division, Office of Basic Energy Sciences, and the Humboldt Foundation (U.T.); and Deutsche Forschungsgemeinschaft Grant SFB/TRR 173 "Spin+X " (to M.A., S. Eich, S. Emmerich, and M.P.).

1. Haight R (1995) Electron dynamics at surfaces. *Surf Sci Rep* 21:275–325.
2. Hertel T, Knoesel E, Wolf M, Ertl G (1996) Ultrafast electron dynamics at Cu(111): Response of an electron gas to optical excitation. *Phys Rev Lett* 76:535–538.
3. Bauer M, Marienfeld A, Aeschlimann M (2015) Hot electron lifetimes in metals probed by time-resolved two-photon photoemission. *Prog Surf Sci* 90:319–376.
4. Schmuttenmaer CA, et al. (1994) Time-resolved two-photon photoemission from Cu(100): Energy dependence of electron relaxation. *Phys Rev B Condens Matter* 50: 8957–8960.
5. Aeschlimann M, et al. (1997) Ultrafast spin-dependent electron dynamics in fcc Co. *Phys Rev Lett* 79:5158–5161.
6. Knorren R, Bennemann KH, Burgermeister R, Aeschlimann M (2000) Dynamics of excited electrons in copper and ferromagnetic transition metals: Theory and experiment. *Phys Rev B* 61:9427–9440.
7. Rudolf D, et al. (2012) Ultrafast magnetization enhancement in metallic multilayers driven by superdiffusive spin current. *Nat Commun* 3:1037.
8. Mathias S, et al. (2012) Probing the timescale of the exchange interaction in a ferromagnetic alloy. *Proc Natl Acad Sci USA* 109:4792–4797.
9. Hellmann S, et al. (2012) Time-domain classification of charge-density-wave insulators. *Nat Commun* 3:1069.
10. Nessler W, et al. (1998) Femtosecond time-resolved study of the energy and temperature dependence of hot-electron lifetimes in $Bi_2Sr_2CaCu_2O_{8+\delta}$. *Phys Rev Lett* 81: 4480–4483.
11. Perfetti L, et al. (2007) Ultrafast electron relaxation in superconducting Bi(2)Sr(2)CaCu(2)O(8+δ) by time-resolved photoelectron spectroscopy. *Phys Rev Lett* 99:197001.
12. Huber R, et al. (2001) How many-particle interactions develop after ultrafast excitation of an electron-hole plasma. *Nature* 414:286–289.
13. Lindhard J (1954) On the properties of a gas of charged particles. *Mat Fys Medd K Dan Vidensk Selsk* 28:37.
14. Quinn JJ, Ferrell RA (1958) Electron self-energy approach to correlation in a degenerate electron gas. *Phys Rev* 112:812–827.
15. Landau LD (1957) The theory of a Fermi liquid. *Sov Phys JETP* 3:920–925.
16. Landau LD (1957) Oscillations in a Fermi liquid. *Sov Phys JETP* 5:101–108.
17. Campillo I, Pitarke JM, Rubio A, Zarate E, Echenique PM (1999) Inelastic lifetimes of hot electrons in real metals. *Phys Rev Lett* 83:2230–2233.
18. Echenique PM, Pitarke JM, Chulkov EV, Rubio A (2000) Theory of inelastic lifetimes of low-energy electrons in metals. *Chem Phys* 251:1–35.
19. Ladstädter F, Hohenester U, Puschnig P, Ambrosch-Draxl C (2004) First-principles calculation of hot-electron scattering in metals. *Phys Rev B* 70:235125.
20. Aryasetiawan F, et al. (2004) Frequency-dependent local interactions and low-energy effective models from electronic structure calculations. *Phys Rev B* 70:195104.
21. Aryasetiawan F, Karlsson K, Jepsen O, Schönberger U (2006) Calculations of Hubbard U from first-principles. *Phys Rev B* 74:125106.
22. Springer M, Aryasetiawan F (1998) Frequency-dependent screened interaction in Ni within the random-phase approximation. *Phys Rev B* 57:4364–4368.
23. Rundquist A, et al. (1998) Phase-matched generation of coherent soft X-rays. *Science* 280:1412–1415.
24. Zhang CH, Thumm U (2009) Laser-assisted photoemission from adsorbate-covered metal surfaces: Time-resolved core-hole relaxation dynamics from sideband profiles. *Phys Rev A* 80:32902.
25. Miaja-Avila L, et al. (2006) Laser-assisted photoelectric effect from surfaces. *Phys Rev Lett* 97:113604.
26. Pazourek R, Nagele S, Burgdörfer J (2015) Attosecond chronoscopy of photoemission. *Rev Mod Phys* 87:765–802.
27. Schultze M, et al. (2010) Delay in photoemission. *Science* 328:1658–1662.
28. Klünder K, et al. (2011) Probing single-photon ionization on the attosecond time scale. *Phys Rev Lett* 106:143002.
29. Locher R, et al. (2015) Energy-dependent photoemission delays from noble metal surfaces by attosecond interferometry. *Optica* 2:405–410.
30. Paul PM, et al. (2001) Observation of a train of attosecond pulses from high harmonic generation. *Science* 292:1689–1692.
31. Zhang C-H, Thumm U (2010) Electron-ion interaction effects in attosecond time-resolved photoelectron spectra. *Phys Rev A* 82:43405.
32. Bovensiepen U, Ligges M (2016) PHYSICS. Timing photoemission–Final state matters. *Science* 353:28–29.
33. Tao Z, et al. (2016) Direct time-domain observation of attosecond final-state lifetimes in photoemission from solids. *Science* 353:62–67.
34. Hermanson J (1977) Final-state symmetry and polarization effects in angle-resolved photoemission spectroscopy. *Solid State Commun* 22:9–11.
35. Hüfner S (2003) *Photoelectron Spectroscopy: Principles and Applications* (Springer, Berlin), 3rd Ed.
36. Roth F, Lupulescu C, Darlatt E, Gottwald A, Eberhardt W (2016) Angle resolved photoemission from Cu single crystals: Known facts and a few surprises about the photoemission process. *J Electron Spectrosc Relat Phenom* 208:2–10.
37. Goldmann A, Altmann W, Dose V (1991) Experimental widths of excited electron states in metals. *Solid State Commun* 79:511–514.
38. Gurtubay IG, Pitarke JM, Echenique PM (2004) Exchange and correlation effects in the relaxation of hot electrons in noble metals. *Phys Rev B* 69:245106.
39. Kliewer J, et al. (2000) Dimensionality effects in the lifetime of surface states. *Science* 288:1399–1402.
40. García-Lekue A, Pitarke JM, Chulkov EV, Liebsch A, Echenique PM (2003) Role of occupied d bands in the dynamics of excited electrons and holes in Ag. *Phys Rev B* 68: 45103.
41. Quinn JJ (1963) The range of hot electrons and holes in metals. *Appl Phys Lett* 2: 167–169.
42. Quinn JJ (1962) Range of excited electrons in metals. *Phys Rev* 126:1453–1457.
43. Borisov A, Sánchez-Portal D, Muiño RD, Echenique PM (2004) Building up the screening below the femtosecond scale. *Chem Phys Lett* 387:95–100.

44. Berglund CN, Spicer WE (1964) Photoemission studies of copper and silver: Theory. *Phys Rev* 136:A1030–A1044.
45. Penn DR, Apell SP, Girvin SM (1985) Theory of spin-polarized secondary electrons in transition metals. *Phys Rev Lett* 55:518–521.
46. Zarate E, Apell P, Echenique PM (1999) Calculation of low-energy-electron lifetimes. *Phys Rev B* 60:2326–2332.
47. Ehrenreich H, Philipp HR (1962) Optical properties of Ag and Cu. *Phys Rev* 128:1622–1629.
48. Knorren R, Bouzerar G, Bennemann K (2001) Dynamics of excited electrons in copper: The role of Auger electrons. *Phys Rev B* 63:94306.
49. Baibich MN, et al.; Nguyen Van Dau F (1988) Giant magnetoresistance of (001)Fe/(001)Cr magnetic superlattices. *Phys Rev Lett* 61:2472–2475.
50. Miller DL, Keller MW, Shaw JM, Chiaramonti AN, Keller RR (2012) Epitaxial (111) films of Cu, Ni, and Cu_xNi_y on α-Al_2O_3 (0001) for graphene growth by chemical vapor deposition. *J Appl Phys* 112:64317.
51. Himpsel FJ, Eberhardt W (1979) High energy final bands in Cu. *Solid State Commun* 31:747–749.
52. Chiang T-C, Knapp JA, Aono M, Eastman DE (1980) Angle-resolved photoemission, valence-band dispersions E(k), and electron and hole lifetimes for GaAs. *Phys Rev B* 21:3513–3522.
53. Thiry P, et al. (1979) E vs k and inverse lifetime of Cu (110). *Phys Rev Lett* 43:82–85.
54. Kresse G, Furthmüller J (1996) Efficient iterative schemes for *ab initio* total-energy calculations using a plane-wave basis set. *Phys Rev B Condens Matter* 54:11169–11186.
55. Kresse G, Furthmüller J (1996) Efficiency of ab-initio total energy calculations for metals and semiconductors using a plane-wave basis set. *Comput Mater Sci* 6:15–50.
56. Blöchl PE (1994) Projector augmented-wave method. *Phys Rev B Condens Matter* 50: 17953–17979.
57. Kresse G, Joubert D (1999) From ultrasoft pseudopotentials to the projector augmented-wave method. *Phys Rev B* 59:1758–1775.
58. Perdew JP, Wang Y (1992) Accurate and simple analytic representation of the electron-gas correlation energy. *Phys Rev B Condens Matter* 45:13244–13249.
59. Lobo-Checa J, et al. (2008) Hidden surface states on pristine and H-passivated Ni(111): Angle-resolved photoemission and density-functional calculations. *Phys Rev B* 77: 75415.
60. Hasegawa M, Nishidate K, Hosokai T, Yoshimoto N (2013) Electronic-structure modification of graphene on Ni(111) surface by the intercalation of a noble metal. *Phys Rev B* 87:85439.
61. Matyba P, et al. (2015) Controlling the electronic structure of graphene using surface-adsorbate interactions. *Phys Rev B* 92:041407.
62. Monkhorst HJ, Pack JD (1976) Special points for Brillouin-zone integrations. *Phys Rev B* 13:5188–5192.
63. Methfessel M, Paxton AT (1989) High-precision sampling for Brillouin-zone integration in metals. *Phys Rev B Condens Matter* 40:3616–3621.
64. Haynes WM, ed (2014) *CRC Handbook of Chemistry and Physics* (CRC, Boca Raton, FL).
65. Segall B (1962) Fermi surface and energy bands of copper. *Phys Rev* 125:109–122.
66. Burdick GA (1963) Energy band structure of copper. *Phys Rev* 129:138–150.
67. Moruzzi VL, Janak JF, Williams AB (1978) *Calculated Electronic Properties of Metals* (Pergamon, New York).
68. Perdew JP, Burke K, Ernzerhof M (1996) Generalized gradient approximation made simple. *Phys Rev Lett* 77:3865–3868.
69. Vanderbilt D (1990) Soft self-consistent pseudopotentials in a generalized eigenvalue formalism. *Phys Rev B Condens Matter* 41:7892–7895.
70. Giannozzi P, et al. (2009) QUANTUM ESPRESSO: A modular and open-source software project for quantum simulations of materials. *J Phys Condens Matter* 21:395502.
71. Krolikowski WF, Spicer WE (1969) Photoemission studies of the noble metals. I. Copper. *Phys Rev* 185:882–900.
72. Penn DR, Apell SP, Girvin SM (1985) Spin polarization of secondary electrons in transition metals: Theory. *Phys Rev B Condens Matter* 32:7753–7768.
73. Kane EO (1967) Electron scattering by pair production in silicon. *Phys Rev* 159: 624–631.
74. Zhukov VP, Aryasetiawan F, Chulkov EV, Echenique PM (2002) Lifetimes of quasiparticle excitations in 4d transition metals: Scattering theory and LMTO-RPA-GW approaches. *Phys Rev B* 65:115116.
75. Zhukov VP, Chulkov EV (2002) Lifetimes of low-energy electron excitations in metals. *J Phys Condens Matter* 14:1937–1947.

Supporting Information

Chen et al. 10.1073/pnas.1706466114

SI Methods

In *Supporting Information* we first discuss the experimental setup and sample preparation in section S1. Next, we show and analyze the static ARPES spectra of Cu(111) and Cu(100) measured by a He discharge lamp in section S2 and by our HHG light source in section S3. Details about the time-resolved data collection and analysis are shown in section S4 and angle-dependent data extraction and analysis in section S5. In section S6, we present details about the DFT calculations used in our work. The DFT-calculated DOS are used to numerically calculate the spin-dependent scattering rate, which we show in detail in section S7. Finally, in section S8, we discuss an approximation of the *d*-electron screening effects.

S1. Experimental Setup and Sample Preparation

Fig. S1*A* shows our experimental setup. We use a single-stage Ti: sapphire multipass amplifier to generate 26-fs near- IR pulses with an energy of 2.4 mJ, at 4-kHz repetition rate and at a central wavelength of 780 nm. Approximately 95% of the output energy is used to produce attosecond EUV pulse trains through HHG. The remaining 5% of the IR pulses is used to probe (dress) the photoelectrons generated by the attosecond pulse trains. In HHG, the IR beam is focused into a 150-μm-diameter, 1-cm-long gas-filled capillary waveguide using a 50-cm-focal-length lens. We use different noble gas targets (Xe, Kr, and Ar) to cover a broad range of EUV photon energies from 16 to 42 eV (corresponding to HHG orders 11–27). The EUV beam has the same polarization as the fundamental IR driving field, which can be adjusted from s to p using a λ/2 waveplate and polarizer. This ability to control the EUV polarization allows us to selectively excite photoelectrons from different initial states into different final states (either free-electron-like or unoccupied excited bulk bands) and study their individual lifetime (Figs. 1*C*, 2*A*, and 4 in the main text). The attosecond pulse trains are then focused onto an atomically clean metal surface [Cu(111) or Cu(001)] using a toroidal mirror (coated with B4C or Au depending on the energy range of EUV light used) at a grazing incidence, to a spot size of ∼100 μm FWHM. The driving IR laser beam is blocked using a 0.2-μm Al filter.

We use laser-assisted photoemission and RABBITT to measure the photoelectron lifetimes for different initial and final states. In our experiment (Fig. S1*A*), the linearly polarized IR probe beam is recombined collinearly with the EUV beam using an annular silver mirror. The IR beam is 250-μm FWHM in diameter with a peak intensity of 2.8×10^{11}W/cm^2, which is optimized to produce a single laser-assisted sideband on the photoelectron spectrum [higher dressing laser intensities could produce higher-order (≥2) sidebands and space-charge distortion of the photoelectron spectrum]. The polarization of the IR probe beam is p-polarized for all our measurements. In the presence of both the attosecond pulse train and the dressing laser field there are two distinct quantum paths for photoelectrons originating from the same initial occupied state to the same final state (sideband), namely (*i*) absorbing an HHG and an IR photon $\hbar\omega_{2n-1} + \hbar\omega_L$ and (*ii*) absorbing the next higher-order HHG photon and emitting an IR photon $\hbar\omega_{2n+1} - \hbar\omega_L$, as shown in Fig. S1*B*. The interference between these two quantum paths induces oscillations on the photoelectron spectrum as a function of time delay between the HHG and IR laser fields, with frequency $2\omega_L$. The photoelectron lifetime is encoded in this oscillation phase along with the phase of the harmonic field (33). The simultaneous measurement of two states excited by the same harmonic orders allows us to cancel the influence of harmonic phase and retrieve the photoelectron lifetime from individual states (28). The measurements on both Cu and Ni were conducted at the room temperature.

The Cu(111) and Cu(001) samples used in our experiment are commercially available single crystals (diameter 10 mm × thickness 2 mm; Princeton Scientific Corp.) with surface polish roughness of <10 nm and orientation accuracy <0.1°. (Certain commercial instruments are identified to specify the experimental study adequately. This does not imply endorsement by NIST or that the instruments are the best available for the purpose.) Sample cleaning is performed in the same UHV chamber used for the photoemission measurements, with a base pressure $<5 \times 10^{-10}$ torr. The cleaning procedure for both crystal surfaces follows the same sequence of repeated cycles of Ar ion sputtering (beam energy 0.7keV) at room temperature and subsequent annealing to 820 K. For the Cu(111) single crystal, the Shockley surface state can be clearly distinguished for an atomically clean surface. The samples are electrically grounded during all static and dynamic measurements.

The Ni(111) single-crystal films are prepared by sputtering 200 nm of nickel onto α-Al_2O_3(0001) substrates as described in ref. 50. In the ARPES UHV chamber, where the pressure during measurements is kept $<5 \times 10^{-10}$ torr, the atomically clean Ni(111) surface is obtained using repeated cycles of Argon ion sputtering (0.5 keV, incidence angle of 60°) at room temperature (300 K) in the UHV chamber, followed by annealing to 900 K for 15 min. The sample is grounded during all static and dynamic measurements.

S2. Static ARPES Spectra of Cu(111) and Cu(001)

We measure the static spectra of the sample at the room temperature using a helium discharge lamp (Specs UVS300, unpolarized radiation). Cu(111) is measured using the He Iα line at 21.2 eV, which can clearly visualize the surface state. The static spectra of Cu(001) surface is obtained using the He II line at 40.8 eV, which is near the HHG photon energy range used in time-resolved experiment on Cu(001). The spectra are recorded with a hemispherical angle-resolved electron analyzer (Specs Phoibos 100; acceptance angle is ±15° under wide-angle mode) and taken along the $\overline{\Gamma}$–$\overline{K}$ direction of the surface BZ for the Cu(111) surface, and along the $\overline{\Gamma}$–$\overline{X}$ direction for the Cu(001) surface. During the measurement, the sample is mounted on a XYZ manipulator with azimuthal angle adjustment so that the crystal orientation and position of the pump and probe beams can be adjusted.

Fig. S2*A* shows the band structure of Cu(111) along $\overline{\Gamma}-\overline{K}$ measured using the He Iα source. The Cu(111) single crystal features a Shockey surface state at ∼0.4eV below the Fermi surface. In terms of the bulk bands, all of the original Λ bands along the Γ–L direction evolve into Σ bands along the $\overline{\Gamma}-\overline{K}$ direction. The Λ_3^α band with a binding energy ∼2.8 eV splits into Σ_1^α and Σ_4 bands. The lower Λ_3^β and Λ_1 bands with binding energies around 3.6 eV evolve into Σ_1^β, Σ_2, and Σ_3 bands. Due to the wavefunction symmetry of these bands they can be selectively excited with polarized HHG light (34).

The band structure of Cu(001) along $\overline{\Gamma}-\overline{X}$ measured using a He II line is plotted in Fig. S2*B*. Because emission from the Γ-point of the bulk band structure in Cu(001) occurs at photon energy around 41 eV, which is close to the He II 40.8eV photon energy, Fig. S2*B* manifests the transition along the Δ axis of the bulk BZ (36, 51). The two degenerate upper bands at the Γ-point

with binding energy ~2.9 eV are Δ_1 and Δ_2 bands. The lower two bands crossing at the Γ-point with binding energy ~3.7 eV are $\Delta_{2'}$ and Δ_5 bands. These two lower bands both exhibit double components due to spin-orbit splitting. In the normal emission geometry, photoemission from bands with a Δ_2 geometry is forbidden due to selection rules, allowing us to unambiguously extract the photoemission delay between the Δ_1 and Δ_5 bands.

S3. Static HHG Photoelectron Spectra Analysis of Cu(111)

The band dispersions of Cu(111) along the Γ–L direction are extracted from the HHG-excited photoelectron spectra in a normal emission geometry. We first obtain the photoelectron energy distribution curves (EDCs) by integrating the angle-resolved spectra over an angle of ±2° around the $\bar{\Gamma}$ point and deduct the secondary electron background using the Shirley background subtraction (52). The energy of the Fermi level of each EDC is determined with the knowledge of the photon energies and the analyzer work function. By using the good energy resolution of attosecond pulse trains and photoemission selection rules for s- and p-polarized HHG beams, we can unambiguously identify the peaks corresponding to different initial states. According to the DFT band-structure calculation for a Cu(111) single crystal, there are three bands along Γ–L that contribute to the photoemission spectra: two valence bands with Λ_3 symmetry (Λ_3^α with lower binding energy of ~2.8 eV and Λ_3^β with higher binding energy of ~3.5 eV) and one deeper valence band with Λ_1 symmetry (~3.8 eV). Because the Λ_1 band can only be excited by a light polarized perpendicular to the sample surface (34, 35), we can assign the two spectral peaks in the EDCs excited by s-polarized HHG light as photoelectrons from Λ_3^α and Λ_3^β bands. We then use a double Voigt function to fit the EDCs and extract their spectra intensity and binding energy, as shown in Fig. S3 *A* and *B*. The Gaussian linewidths of the Voigt function are set to the experimental resolution of ≈0.3 eV. The band-mapping results are plotted in Fig. 1*B*, showing good agreement with the band structure obtained from DFT calculations. To extract information about the Λ_1 band, the EDCs excited by the same harmonic orders but with different polarizations (s- and p-) are normalized to equalize the intensity of the Λ_3^α band. The additional spectral weight in the photoelectron spectra excited by p-polarized HHG is assigned as photoemission from the Λ_1 band. We obtain its spectral intensity and binding energy by fitting it with a single Voigt function, as shown in Fig. S3 *C* and *D*. The extracted band-structure of Cu(111) along the Γ–L direction is plotted in Fig. 1*B*. The inner potential of Cu(111) is 8.6 eV according to previous photoemission studies (53).

To determine which initial bands are coupled to which unoccupied final bands and also the linewidth of the final bands (Fig. 2*B* in the main text), we examine the dependence of the intensity of individual photoemission peaks on the photon energy. To take into account the intensity modulation of the HHG light, we normalize the intensity of the Λ_3^β and Λ_1 bands to the intensity of the Λ_3^α band. The relative intensities as a function of photon energy are plotted in Fig. S4. We observe a spectral resonance in photoemission from the Λ_3^β band around the 15th order, corresponding to a resonant transition from the Λ_3^β band to the unoccupied bulk Λ_1^{B} band. In contrast, the intensity of photoemission from the Λ_1 band varies smoothly across the same energy range.

S4. Time-Resolved Data Collection and Analysis

To improve the signal-to-noise ratio and minimize any systematic error, the same pump-probe delay sequence from −3 fs to 3 fs in 0.2-fs steps is repeated more than 200 times with increasing and decreasing delays alternating between consecutive scans. Each individual photoelectron spectrum in the time-resolved measurements is integrated for 4–6 s to accumulate sufficient photoelectron counts. To minimize space charge effects, the photoelectron counts are adjusted well below the point where further reduction in HHG light intensity does not shift the spectra. The repetitive scans are analyzed individually and then averaged to obtain the photoemission delays. The error bars are determined by considering the variation of measured time delays in individual scans, including those where the HHG light is generated using different noble-gas targets.

To cover as large a photon energy range as possible, different noble gases (Xe, Kr, and Ar) are used for HHG. The same sideband regions (SB 14, 16, 18, and 20) can be reached by Xe and Kr gases, as shown in Fig. S5. The fact that we observe consistent results for all gases indicates that the phase delay of the HHG field itself is cancelled out in our measurement, and therefore the observed time delay originates only from the intrinsic material properties. For Cu(001) only SB 18–26 are probed, because the energy separation between Δ_5 and Δ_1 becomes too small to resolve at lower energies.

We have checked the data quality by examining several factors. (*i*) We confirm that the peak positions in each spectrum corresponding to different initial bands are not altered because of space charge effects, above-threshold ionization by IR field, or a shift in high harmonic photon energies. (*ii*) Each sideband region of interest in every scan shows a dominant $2\omega_L$ (ω_L is the fundamental laser frequency) oscillation in Fourier analysis. The interferograms shown in Figs. 2*D* and 3*B* in the main text are obtained by summing the interferograms of individual scans satisfying the two criteria above.

To extract the 1D lineouts corresponding to the RABBITT oscillations for different initial bands [Λ_3^α,Λ_3^β bands for Cu(111) surface, Δ_1 and Δ_5 bands for Cu(001) surface], we integrate the photoelectron counts over a spectral window with an energy width of 300 meV and an angle width of ±2.5° centered at the $\bar{\Gamma}$ point of the sideband peak corresponding to the band of interest. The counts are plotted as a function of the pump-probe delay (τ_d), yielding 1D lineouts.

S5. Angle-Dependent Data Extraction and Analysis

To extract the angle-dependent photoemission time delay we first divide the angle-resolved photoemission spectra into 16 angular regions at each sideband, with a ~1.8° angular span over the entire range of photoelectron emission angle ($-15° < \theta < 15°$), as shown in Fig. S6*A*. The photoelectron counts in each region are integrated and plotted as a function of pump-probe time delay τ_d to obtain the angle-dependent RABBITT interferograms. Typical interferograms at the spectral resonance are plotted in Fig. S6 *B* and *C*. In this way, the angle-dependent photoemission time delays for photoelectrons originating from different bands $[\tau_{PE}(\Lambda_3^\beta,\theta) - \tau_{PE}(\Lambda_3^\alpha,\theta)]$ can be extracted for Cu(111).

As illustrated in Fig. 3*C* in the main text, pronounced angle dependence of the photoemission time delay is observed at the spectral resonance (SB 16). In contrast, the photoemission time delay exhibits little angular dependence off resonance (SB 20–26), which indicates that the photoemission delays on and off resonance have different origins.

S6. DFT Band-Structure Calculations

All calculations on Cu were performed using DFT, as implemented in the Vienna Ab-initio Simulation Package (VASP) code (54, 55). Projector augmented wave potentials were used to describe the electron–ion interactions (56, 57), and the exchange-correlation functional was described by the generalized gradient approximation (GGA-PW91) (58). Generalized gradient approximation is a standard method to calculate the band structure of transition metals and compare with ARPES results (59–61). The electron wave function was expanded using plane waves with an energy cutoff of 400 eV in geometry optimization. The BZ of bulk Ni and Cu, containing one atom in the cell, was sampled using (24 × 24 × 24) Γ-centered Monkhorst–Pack k-point mesh (62) together with the Methfessel–Paxton smearing method (63)

using 0.1-eV smearing. Bulk Cu structure was relaxed until the Hellmann–Feynman forces acting on the Cu atom were less than 0.01 eV $Å^{-1}$. Both the energy cutoff and the BZ sampling were tested and the presented values are well-converged. The resulting calculated lattice constant of 3.62 Å agrees well with the experimental value of 3.61 Å (64). For accurate band structure calculations using the optimized geometry, even larger energy cutoffs (1,000 eV) and BZ sampling (48 × 48 × 48) were considered and presented in the paper to ensure convergence for high-energy states. We modeled 24 bands in total (6 occupied and 18 unoccupied) and compared our simulations to available experimental and previous theoretical calculations in different BZ cuts and found similar band structure (65–67). The experimentally relevant final band turned out to be the second-lowest unoccupied band; however, its high energy might raise the possibility of an unphysical ghost state. To test this, we calculated the band structure using PBE functional (68) and Vanderbilt ultrasoft pseudopotentials (69) implemented in Quantum Espresso (70), which showed agreement with our VASP results and previous results (67), excluding the possibility of a ghost state. Calculations for Ni were carried out using parameters similar to those for Cu (33).

S7. Spin-Dependent Scattering Model

The scattering rate between photoelectrons and unexcited bulk electrons is calculated using Fermi's golden rule, following the formulas presented in refs. 6, 45, and 46). Because the unoccupied states above E_F in Ni are electronic states with minority spins (↓), spin-dependent electron–electron scattering needs to be taken into account. The two-electron scattering processes presented in Fig. 4*A* in the main text can be either a spin-conserving or a spin-flipping process for the photoexcited electron. To calculate the total probability of inelastic scattering between two electrons as shown in Fig. 4*A*, the full quantum states of the two-particle initial and final states need to be taken into consideration. The Coulomb matrix element is given by $M^{Ek\sigma,\varepsilon k_1\sigma_1}_{E'k'\sigma',\varepsilon' k_2\sigma_2} \equiv \langle Ek\sigma, \varepsilon k_1\sigma_1|V|E'k'\sigma', \varepsilon' k_2\sigma_2\rangle$, where ($E$, k, σ) and (E', k', σ') are the initial and final states of the photoexcited electron and (ε, k_1, σ_1) and (ε', k_2, σ_2) are the initial and final states of the scattering partner. V is the screened electron–electron interaction. The spin indices σ_1, σ', and σ_2 either equal to σ or are opposite to σ ($\overline{\sigma}$). Specifically, when $\sigma' = \sigma$ the scattering is a spin-conserving process for the photoelectron, whereas if $\sigma' = \overline{\sigma}$, it is a spin-flipping one. The scattering process conserves the total spin-angular momentum of the two-electron system.

In principle, the matrix element $M^{Ek\sigma,\varepsilon k_1\sigma_1}_{E'k'\sigma',\varepsilon' k_2\sigma_2}$ can be calculated by considering the momentums of different states if the wavefunctions and selection rules are known. However, in general this information is not available for allowing accurate calculations in materials. Here, we assume the matrix element is independent to the momenta (k) of both electrons involved in the scattering process (random-***k*** approximation) to investigate the effects of electron–electron scattering on the photoelectron lifetime. The random-***k*** approximation was first used by Berglund and Spicer to calculate the photoemission from Cu and Ag (44) and was later used to calculate electron–electron scattering probability in different materials (6, 71–73). It has been shown that with a proper choice of the momentum-independent matrix element the results obtained from the random-***k*** approximation can be in good agreement with more sophisticated calculations (74, 75). By considering the random-***k*** approximation we can evaluate the electron–electron scattering rate by including the appropriate DOS and Fermi functions. As a result, we can write an averaged matrix element as $M^{E\beta\sigma,\varepsilon\alpha\sigma_1}_{E'\beta\sigma',\varepsilon'\alpha\sigma_2} \equiv \langle E\beta\sigma, \varepsilon\alpha\sigma_1|V|E'\beta\sigma', \varepsilon'\alpha\sigma_2\rangle$, where the energy ($E$), spin ($\sigma$), and orbital character (α, β) of the initial and final states are taken into consideration.

The spin-conserving processes scatter the photoexcited electron from an original state (E, σ) into an unoccupied state (E', σ), and can be formulated as

$$\Gamma^{1)}(E\sigma, E'\sigma) = \frac{\pi}{\hbar}\sum_{\beta=s,p,d}\int_{E_F}^{E} dE' \rho_\sigma^{\beta,>}(E') \times \underbrace{\sum_{\alpha=s,p,d}\int_{E_F-\Delta}^{E_F} d\varepsilon \left[\rho_\sigma^{\alpha,<}(\varepsilon)\rho_\sigma^{\alpha,>}(\varepsilon+\Delta)\left|M^{E\beta\sigma,\varepsilon\alpha\sigma}_{E'\beta\sigma,\varepsilon'\alpha\sigma} - M^{E\beta\sigma,\varepsilon\alpha\sigma}_{\varepsilon'\alpha\sigma,E'\beta\sigma}\right|^2\right.}_{\text{I}} + \underbrace{\left.\rho_{\overline{\sigma}}^{\alpha,<}(\varepsilon)\rho_{\overline{\sigma}}^{\alpha,>}(\varepsilon+\Delta)\left|M^{E\beta\sigma,\varepsilon\alpha\overline{\sigma}}_{E'\beta\sigma,\varepsilon'\alpha\overline{\sigma}}\right|^2\right]}_{\text{II}}, \quad \textbf{[S1]}$$

where $\rho_\sigma^{\alpha,>}$ and $\rho_\sigma^{\alpha,<}$ are given in Eq. **2** in the main text, $\Delta = E - E'$ is the energy transfer between the two electrons and σ_1 can be either σ (same to) or $\overline{\sigma}$ (opposite to photoexcited electron). The first term (I) in the integrand describes the scattering between a photoexcited electron with spin σ and an unexcited electron with the same spin. The fact that electrons are indistinguishable particles is taken into account. The second term (II) describes scattering between the photoexcited electron and an electron with opposite spin ($\overline{\sigma}$). We first neglect the interference term after expanding the modulus square of the matrix elements (72). Then, following ref. 6, we do not further distinguish between *s, p*, and *d* states for the matrix element and assume M is energy-independent. As a result, we only have matrix elements for scattering between electrons with the same spins ($M^{\sigma\sigma}$) and opposite spins ($M^{\sigma\overline{\sigma}}$). We, however, note that an energy-dependent matrix element (M) is obviously observed in current work and other studies, which we will illustrate by using different (but constant throughout energy) values of M to make agreement with low-energy and high-energy results obtained in experiments. Beyond the approach in ref. 6, we assumed that the wavefunction character (*s*, *p*, or *d*) of the initial and final states of an electron are the same during the scattering process. This was suggested by recent all-electron ab initio calculations showing that the scattering rate between two electrons will be vanishingly small if the wavefunction characters of the initial and final states are different (19). For simplicity, we only distinguish between different wavefunctions for the scattering partner in the DOS assignment but do not further distinguish it for the photoexcited electrons. As a result, the DOS used for the final state of photoexcited electrons is the total DOS, $\sum_{\beta=s,p,d}\rho_\sigma^{\beta,>}(E)$.With the considerations above, Eq. **S1** is reduced to

$$\Gamma^{1)}(E\sigma, E'\sigma) = \frac{\pi}{\hbar}\int_{E_F}^{E} dE' \sum_{\beta=s,p,d}\rho_\sigma^{\beta,>}(E') \sum_{\alpha=s,p,d}\int_{E_F-\Delta}^{E_F} d\varepsilon \left[\rho_\sigma^{\alpha,<}(\varepsilon)\rho_\sigma^{\alpha,>}(\varepsilon+\Delta) 2\left|M^{\sigma\sigma}\right|^2 + \rho_{\overline{\sigma}}^{\alpha,<}(\varepsilon)\rho_{\overline{\sigma}}^{\alpha,>}(\varepsilon+\Delta)\left|M^{\sigma\overline{\sigma}}\right|^2\right]. \quad \textbf{[S2]}$$

Similarly, the scattering rate for the spin-flip process is given by

$$\Gamma^{2)}(E\sigma, E'\overline{\sigma}) = \frac{\pi}{\hbar}\int_{E_F}^{E} dE' \sum_{\beta=s,p,d}\rho_{\overline{\sigma}}^{\beta,>}(E') \sum_{\alpha=s,p,d}\int_{E_F-\Delta}^{E_F} d\varepsilon\, \rho_{\overline{\sigma}}^{\alpha,<}(\varepsilon) \times \rho_\sigma^{\alpha,>}(\varepsilon+\Delta)\left|M^{\sigma\overline{\sigma}}\right|^2. \quad \textbf{[S3]}$$

Note that in this process the photoexcited electron must scatter with an unexcited electron with opposite spin to conserve spin-angular momentum in the process. The total scattering rate is hence given by

$$\frac{1}{\tau_\sigma(E)} = \sum_{\sigma'=\sigma,\bar{\sigma}} \Gamma(E\sigma, E'\sigma') = \Gamma^{1)}(E\sigma, E'\sigma) + \Gamma^{2)}(E\sigma, E'\bar{\sigma}), \quad \textbf{[S4]}$$

which yields Eq. **1** in the main text.

It is reasonable to further assume $|M^{\uparrow\uparrow}| = |M^{\downarrow\downarrow}|$, $|M^{\uparrow\downarrow}| = |M^{\downarrow\uparrow}|$ and define $R = |M^{\uparrow\uparrow}/M^{\uparrow\downarrow}|$. For Cu, because the DOS for spin ↑ and spin ↓ are the same, the lifetime of photoexcited electrons is only determined by $M = \sqrt{\frac{1}{2}(|M^{\uparrow\uparrow}|^2 + |M^{\downarrow\downarrow}|^2)}$ and is not related to the value of R. However, for Ni, the lifetimes of spin ↑ and spin ↓ electrons are different and are mainly determined by the value of R. Here, we assume R = 0.5 for Ni, which has been shown to reproduce the experimentally measured lifetime ratio $(\tau_\uparrow/\tau_\downarrow)$ (6).

The spin-dependent *s*, *p*, and *d* DOS of Cu and Ni (Fig. 4*C*, *Inset*) were obtained from DFT calculations and were used to integrate Eq. **1** numerically. As shown in Fig. *4B* in the main text, with M = 1.4 for Cu, the calculated spin-averaged lifetime $\tau = \frac{2\tau_\uparrow\tau_\downarrow}{\tau_\uparrow+\tau_\downarrow}$ is in good agreement with the experimental results measured by atto-ARPES in the high photon energy range (20~40 eV), as well those measured by Tr-2PPE in the low photon energy range (0.5~3.0 eV). We note that our Coulomb matrix element (M) is ~70% larger than the values reported in ref. 6. This is because we confined the initial and final state wavefunction of the scattering partner to be the same, which reduces the available phase space for scattering. In Fig. S7 we show the simulation results without the wavefunction confinement and using the matrix elements in ref. 6 (M = 0.8 for Cu). A similar comparison for Ni is also plotted in Fig. S7, where we also show that the use of different models does not change our major conclusions.

S8. Approximate Estimate of *d*-Electron Screening

As has been discussed in refs. 39 and 41, the effects of *d*-electron screening on the photoexcited electron lifetime can be roughly estimated by an effective dielectric constant $\varepsilon_d = 1 + \delta\varepsilon_d$ and the corrected lifetime is increased by a factor of $\sqrt{\varepsilon_d}$. The values of $\delta\varepsilon_d$ can be directly extracted from experimentally measured optical constants (47), with a vanishingly small contribution at the high energy (>20 eV) as pointed out in ref. 42. The estimated *d*-electron screening effect is plotted as the yellow-colored area in Fig. 4*B*.

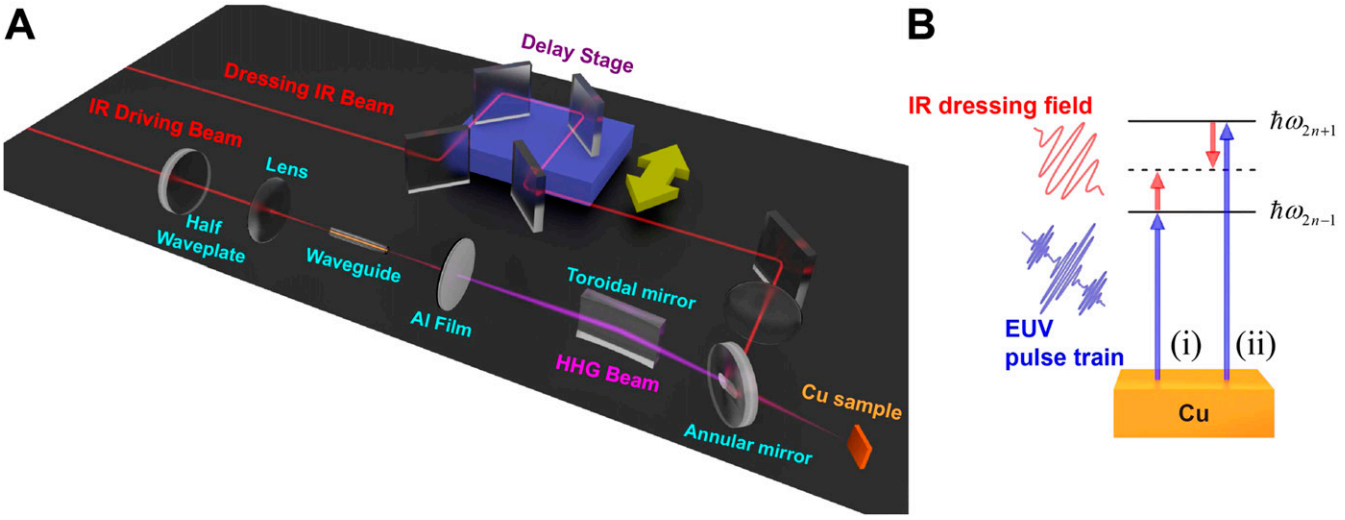

Fig. S1. (*A*) Experimental setup. (*B*) Schematic of quantum path interferences from the same initial state to the same final state using a combined EUV and IR laser fields.

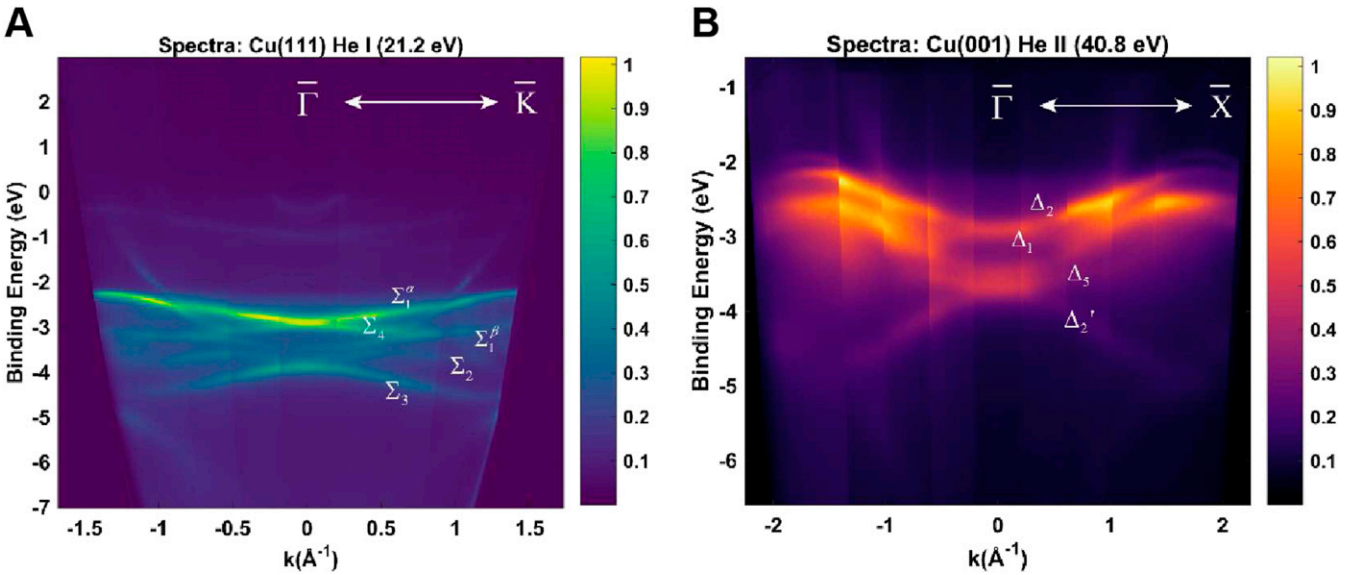

Fig. S2. Photoelectron spectrum of Cu(111) and Cu(001). (*A*) ARPES spectrum of Cu(111) along the $\bar{\Gamma}$–$\bar{K}$ direction taken using the He Iα (21.2eV) line from an He discharge lamp. (*B*) ARPES spectrum of Cu(001) along the $\bar{\Gamma}$–$\bar{X}$ direction taken using the He II (40.8 eV) line from an He discharge lamp.

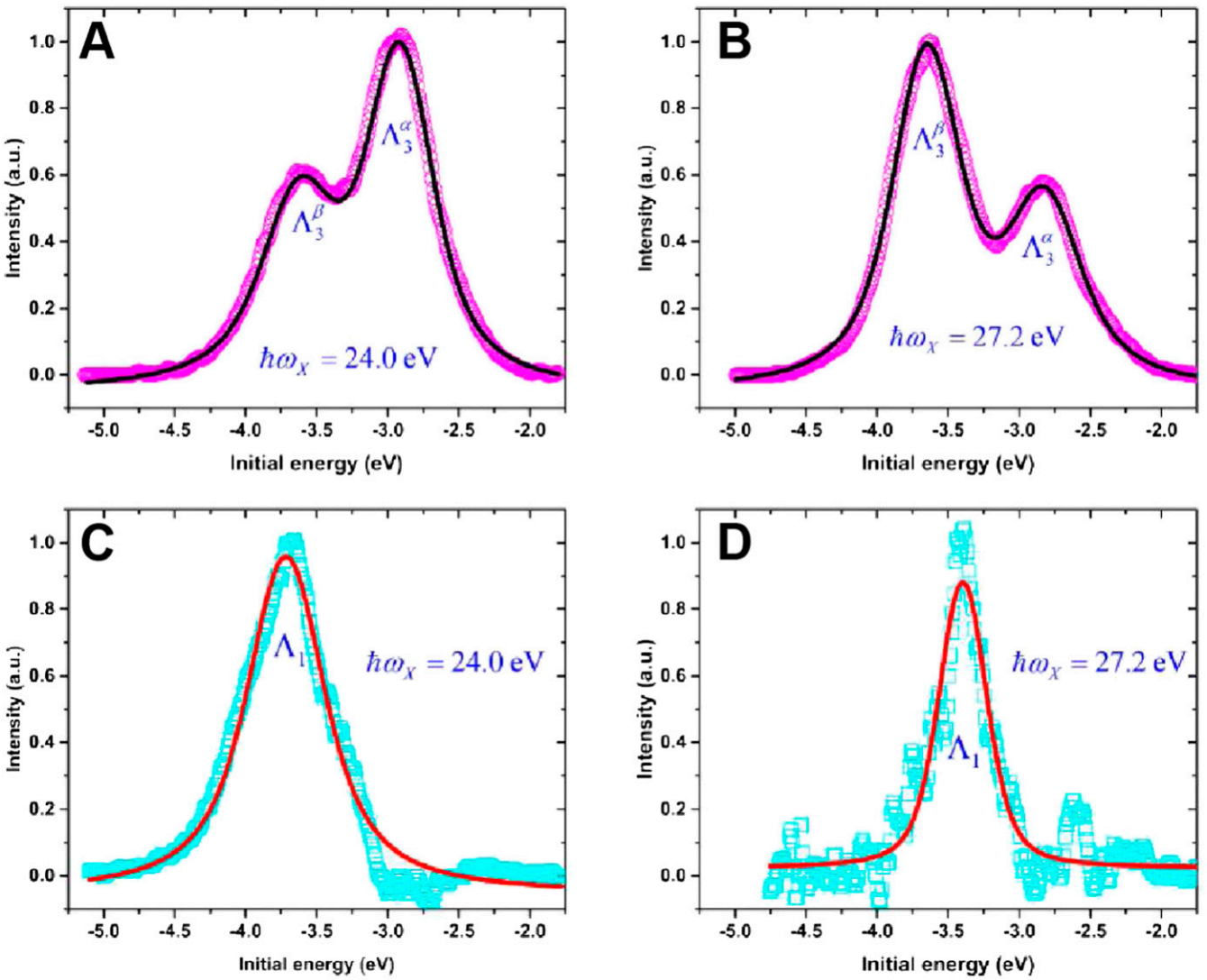

Fig. S3. Static spectral analysis of the Cu(111) surface. (*A* and *B*) Experimentally measured EDCs excited by s-polarized HHG field (magenta open circles). The intensity and binding energies of Λ_3^α and Λ_3^β bands are extracted by fitting the EDCs with double Voigt functions (solid black lines). (*C* and *D*) The spectral intensity of Λ_1 is extracted by taking the difference spectra between EDCs excited by s- and p-polarized HHG fields (open cyan squares). The intensity and binding energies are determined by fitting the EDCs with a single Voigt function (solid red lines).

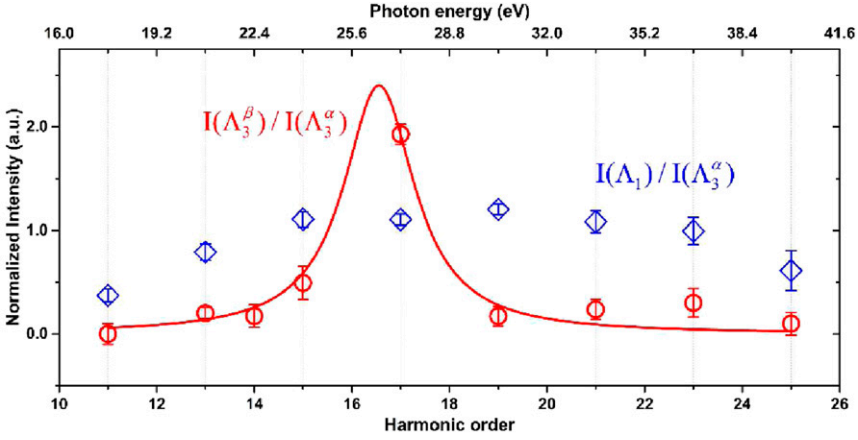

Fig. S4. Spectral intensity of the Λ_3^β and Λ_1 bands. Photoemission intensities of the Λ_3^β (open red circle) and Λ_1 (open blue diamond) bands relative to that of the Λ_3^α band. The solid red line represents the Lorentzian lineshape fit to the intensity of the Λ_3^β band as a function of photon energy, which yields a linewidth of 2.13 $\pm$ 0.65 eV.

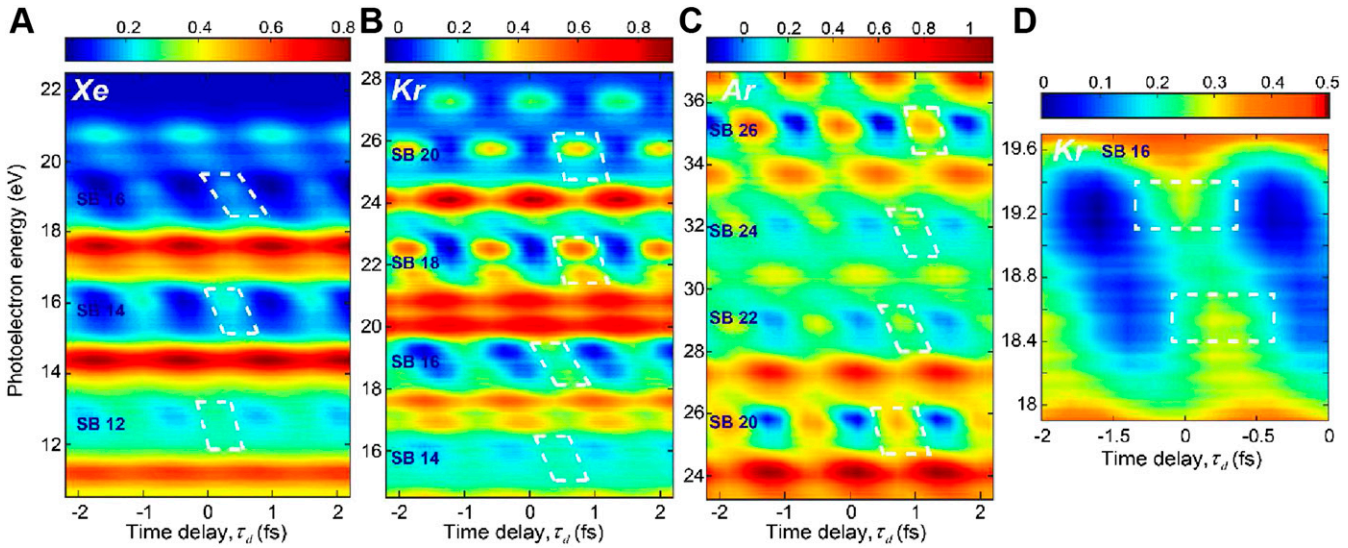

Fig. S5. Interferograms with s-polarized HHG using different noble gas targets. The interferograms covering the resonant energies are obtained by using (*A*) Xe, (*B*) Kr, and (*C*) Ar as gas targets for high-harmonic generation process. The photoemission is excited by s-polarized HHG field. The 11th to 17th HHG orders are covered by Xe, 13th to 21st by Kr, and 19th to 27th by Ar. The oscillation offset at the sidebands is highlighted by white dashed boxes, yielding consistent time delay using different gases. (*D*) A zoom-in view in both energy and time delay at resonance with Kr gas HHG. The white dashed box represents the center of intensity peaks of RABBITT oscillations corresponding to photoelectrons from Λ_3^α and Λ_3^β bands.

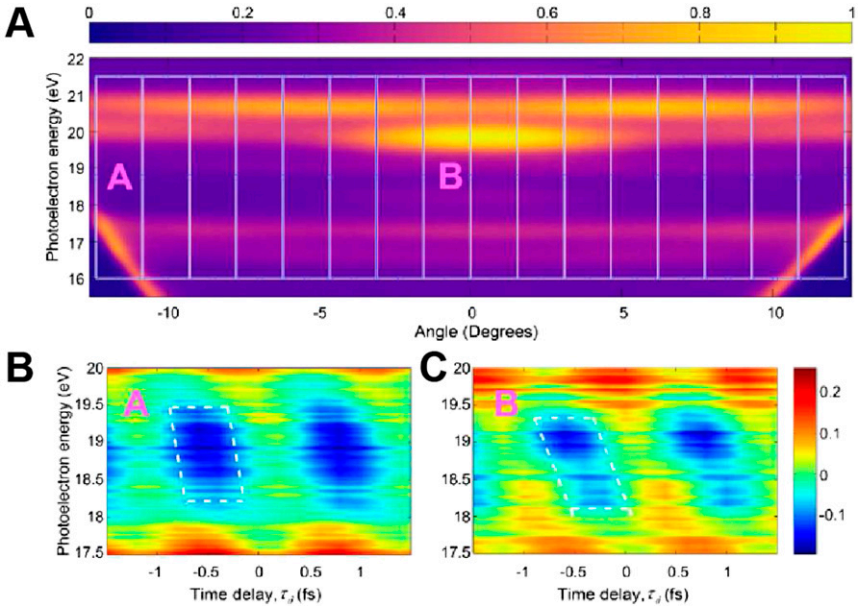

Fig. S6. Angle-dependent photoemission time delay. (*A*) Illustration of the angular regions for integration when extracting the angle-dependent photoemission time delay. The energy region corresponding to SB16 is used as an example here. (*B* and *C*) Typical RABBITT interferograms for SB16 with emission angles (A and B) labeled in *A*. The offset is highlighted with white dashed boxes.

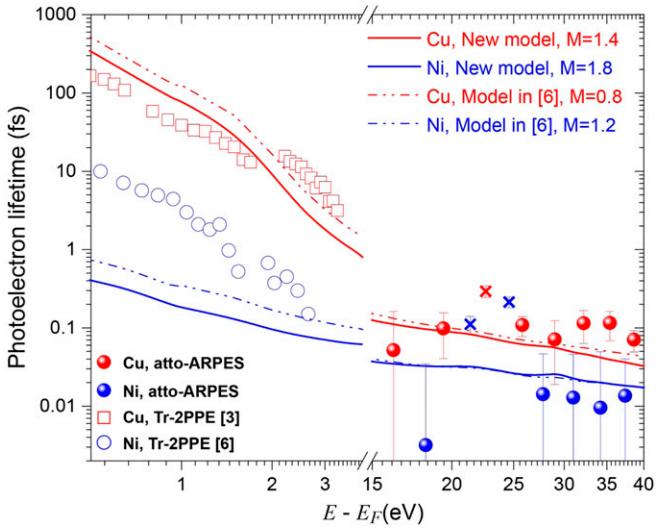

Fig. S7. Effects of wavefunction confinement on the photoelectron lifetime. The simulation results (solid lines) of the "new model" with the wavefunction confinement are plotted in comparison with the model results in ref. 6 (dashed-dotted lines). The results are consistent and the Coulomb matrix element is in general ~70% larger in the new model. The experimental results are plotted as symbols with red for Cu and blue for Ni. The atto-ARPES measured lifetimes on final-state resonance are shown as cross symbols to distinguish them from off-resonant lifetimes.